Long-term observations of black carbon and carbon monoxide in the Poker Flat Research Range, central Alaska, with a focus on forest wildfire emissions

Takeshi Kinase[1], Fumikazu Taketani[1,2], Masayuki Takigawa[1], Chunmao Zhu[2], Yongwon Kim[3], Petr Mordovskoi[1], and Yugo Kanaya[1,2]

[1]Institute of Arctic Climate and Environment Research, Japan Agency for Marine-Earth Science and Technology (JAMSTEC), Yokohama 2360001, Japan
[2]Earth Surface System Research Center, Research Institute for Global Change, Japan Agency for Marine-Earth Science and Technology (JAMSTEC), Yokohama 2360001, Japan
[3]International Arctic Research Center, University of Alaska Fairbanks (UAF), Fairbanks 757340, U.S.A.

Correspondence to: Takeshi Kinase (tkinase@jamstec.go.jp)

Abstract

Forest wildfires in interior Alaska represent an important black carbon (BC) source for the Arctic and sub-Arctic. However, BC observations in interior Alaska have not been sufficient to constrain the range of existing emissions. Here, we show our observations of BC mass concentrations and carbon monoxide (CO) mixing ratios in the Poker Flat Research Range (65.12° N, 147.43° W), located in central Alaska, from April 2016 to December 2020. The medians, 10th, and 90th percentile ranges of the hourly BC mass concentration and CO mixing ratio throughout the observation period were 13, 2.9, and 56 ng m^{-3} and 124.7, 98.7, and 148.3 ppb, respectively. Sporadically large peaks in the BC mass concentration and CO mixing ratio were observed at the same time, indicating influences from common sources. These BC peaks coincided with peaks at other comparative sites in Alaska, indicating large BC emissions in interior Alaska. Source estimation by FLEXPART-WRF confirmed a contribution of boreal forest wildfires in Alaska and western Canada when high BC mass concentrations were observed. For these cases, we found a positive correlation ($r = 0.44$) between the observed BC/ΔCO ratio and fire radiative power (FRP) observed in Alaska and Canada. This finding implies that the variability of the BC and CO emission ratio is associated with the intensity and time progress of forest wildfires and suggests the BC emission factor and/or inventory could be potentially improved by FRP. We recommend that FRP be integrated into future bottom-up emission inventories to achieve a better understanding of the dynamics of pollutants from frequently occurring forest wildfires under the rapidly changing climate in the Arctic.

1 Introduction

Climate change in the Arctic region has been strongly accelerated compared to the global average (Box et al., 2019; Bonfils et al., 2020). The near-surface air temperature increased between 1.8 and 3.1 °C in the period between 1971 and 2017 (Box et al., 2019). This rapid temperature increase in the Arctic region caused decreases in the extent of sea ice (Aizawa et al., 2021), resulting in the acceleration of Arctic warming (Cohen et al., 2014; Thackeray and Hall, 2019). Even if net CO_2 emission is controlled to zero until the end of the 21st century (SSP1-2.6 scenario), modelling studies predicted a more than 3.5 °C temperature increase (Cai et al., 2021; Xie et al., 2022). However, there are still some difficulties associated with climate predictions based on global climate models because of the widespread use of different model hindcasts and forecasts (Overland et al., 2014). Specifically, it is known that the Arctic amplification process causes an acceleration in Arctic warming, but the process is highly complicated and is not sufficiently understood; this includes processes involved in aerosol concentration changes and the deposition of black carbon (BC) on snow and ice surfaces (Cohen et al., 2014). Thus, more research is required to understand Arctic climatic processes.

BC aerosols, which are formed by various incomplete combustion processes, such as fossil fuel and biomass burning (Bond et al., 2013), strongly contribute to warming by absorbing solar radiation (Bond et al., 2013; IPCC, 2021). In addition, BC deposited on snow and ice surfaces decreases surface albedo and contributes to snow melting and warming (Aoki et al., 2011; Bond et al., 2013; Oshima et al., 2020; IPCC, 2021). BC can be transported over long distances (estimated lifetimes are 3–6 days globally (Wang et al., 2014; Lund et al., 2018)) and affect the climate and environment of remote regions, such as the Arctic (Wang et al., 2011; Matsui et al., 2022). However, large discrepancies among model estimations for BC climate effects on the Arctic remain (Gliß et al., 2021) because of a lack of observation data (IPCC, 2021) to constrain the models in terms of dependence on emission inventories (Pan et al., 2020; Matsui et al., 2022) and/or removal rates (Ikeda et al., 2017; Lund et al., 2018). For long-range transport from Asia to the Arctic, constraints on the major BC emissions from East Asia (Choi et al., 2020; Kanaya et al., 2020), ship-based observations for BC transport to the Arctic (Taketani et al., 2016, 2022), evaluation of the multimodel bias using these datasets (Whaley et al., 2022) and an improved understanding of transport mechanisms and source attributions (Ikeda et al., 2017; Zhu et al., 2020) have been achieved. However, more observational constraints are required for the characterization of BC emissions from boreal forest wildfires (Pan et al., 2020; AMAP, 2021).

Forest wildfires in the northern American region, especially those that occur in Alaska every summer (Picotte et al., 2020), are one of the important BC emission sources in the Arctic and subarctic troposphere, and they result in depositional fluxes on snow and ice over the Arctic and surrounding regions (Xu et al., 2017; AMAP, 2021; Matsui et al., 2022). The occurrences of these forest wildfires in interior Alaska have increased since the 1980s (Sierra-Hernández et al., 2022), and this increasing trend is predicted to continue (Hu et al., 2015; Box et al., 2019; AMAP, 2021); the emission of aerosols, including BC from forest wildfires, is projected to severely affect the environment (Halofsky et al., 2020) and climate (Schmale et al., 2021) in the future.

BC mass concentrations have long been observed in the atmosphere and snow at Utqiagvik (Barrow) (Eck et al., 2009; Garrett et al., 2011; Mori et al., 2020), which is a high Arctic coastal tundra site. Campaign studies on atmospheric BC mass concentrations were also conducted in interior Alaska using aircrafts (Kondo et al., 2011b; Bian et al., 2013; Creamean et al., 2018). These campaign observations have provided an in-depth understanding of aerosol parameters related to wildfires. However, separate long-term observations of BC mass concentrations are required to characterize annual trends and seasonality. Fewer studies have reported atmospheric BC mass concentrations in interior and coastal Alaska (Polissar et al., 1996, 1998; Eck et al., 2009; Mouteva et al., 2015) and the high Arctic coastal site (Alert, Canada) (Garrett et al., 2011). To understand the long-term variations in BC mass concentration and their impacts on the climate and environment, more BC observation data from interior Alaska are needed (AMAP, 2011). In this study, we aimed to investigate detailed variations in BC mass concentration and its sources, with a focus on forest wildfires in interior Alaska, based on our monitoring of BC and CO at the Poker Flat Research Range (PFRR), which is a University of Alaska Fairbanks (UAF) observational site in interior Alaska.

2 Method

2.1 Observation site

We conducted BC and CO monitoring at the PFRR (65.12° N, 147.43° W, 500 m a.s.l.) starting in April 2016. The PFRR is located in the centre of interior Alaska (Figure 1), approximately 35 km northeast of Fairbanks. The PFRR is surrounded by a predominant evergreen needled-leaved (black spruce; *Picea mariana*) forest with shrubland and herbaceous vegetation (Buchhorn et al., 2020). Note, that the effects of deposition by trees and canopies can be ignored because the laboratory is located on a mountain hill, with non-tall (~2m) sparse black spruce forest. In this study, BC and CO monitoring results were analysed between April 2016 and December 2020.

83
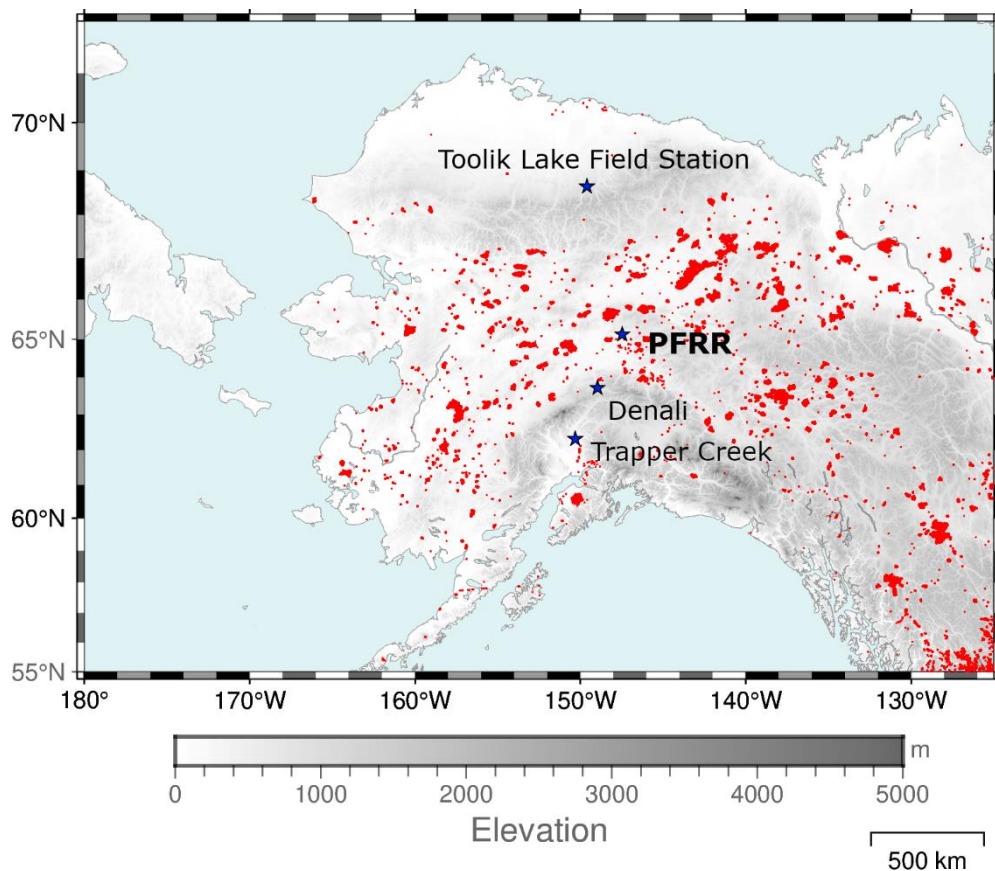
Figure 1. A map that shows the location of the PFRR and other sites compared in Section 3.2 (Trapper Creek, Denali, and
Toolik Lake Field Station). All hot spots (larger than 0.3 (MW) in fire radiative power (FRP)) observed in the USA and Canada
by the Visible Infrared Imaging Radiometer Suite (VIIRS) between 2016 and 2020 are shown in red colour.

87

2.2 Measurements

BC was measured by a Continuous Soot Monitoring System (BCM3130, Kanomax, Japan) with a flow rate of 0.78 L min^{-1} at
standard temperature and pressure (STP; 273 K and 1013 hPa). Sample air was introduced using an approximately 10 m
conductive silicone tube (1/2″ i.d.) from a height of 5.5 m above the ground. The measurement technique of BCM3130 is
based on filter-based optical absorption, thus other light-absorbing particles and scattering particles can be a source of
interferences on BC measurement (Bond et al., 1999; Kondo et al., 2009). To minimize interferences from these particles,
coarse mode particles (approximately >1.0 µm), such as mineral dust, were removed by a PM$_{1.0}$ cyclone (URG-2000-30ED,

95 URG, USA) operated with a small flow regulation pump (~4.5 L min^{-1} at STP). Note, as most BC particles are smaller than 1

96 µm (Bond et al., 2013), BC loss through the PM$_{1.0}$ cyclone can be ignored. In addition, to remove nonrefractory particles, such

97 as sulfate and organics, the sample air was heated to approximately 300 °C using a heated inlet before it was introduced into

98 the instrument. More details of the instrument are described elsewhere (Miyazaki et al., 2008; Kondo et al., 2009, 2011a). One-

99 minute observation data were averaged to hourly data as the primary data. The limit of detection value (LOD) for hourly BC

100 mass concentration was estimated to be 2 ng m^{-3}, which is the sum of average hourly data and 3-σ values using 18 hours of

101 particle-free air measurements.

102 The CO mixing ratio was measured by an infrared absorption photometer (48iTLE, Thermo Fisher Scientific, USA) with a

103 flow rate of 0.5 L min^{-1}. Sample air was introduced using an approximately 10 m PFA tube from a height of 5.5 m above the

104 ground. Internal zero measurements were carried out for 20 minutes every hour, and the CO mixing ratio was estimated from

105 the difference in absorption between the sample and the zero measurements. Span gas (0.99 ppm CO/N$_2$, Taiyo-Nissan, Tokyo,

106 Japan) calibration was performed in April 2016. We calculated ΔCO as the enhancement in CO from background levels (14

107 days moving 5-percentile values of observation results). Cases with hourly ΔCO larger than 3-σ (13.9 ppb in median, 1-σ was

108 derived from zero mode measurements before and after the hourly ambient air observations) were only used for analysis. To

109 validate our CO observations, we compared our observed CO mixing ratio with aircraft observations (less than 500 m AGL

110 above the PFRR) provided by the NOAA Global Monitoring Laboratory (https://doi.org/10.15138/39HR-9N34; accessed on

111 2 November 2023) (Figure S1), confirming a good agreement between these two observation results.

112

113 **2.3 Model calculation**

114 The FLEXPART (FLEXible PARTicle dispersion model)-WRF (Weather Research & Forecast) model was used in backward

115 mode to characterize the source areas and sectors for the sampled air masses at the PFRR. FLEXPART-WRF version 3.3

116 (Brioude et al., 2013) and WRF version 4.4 (Skamarock et al., 2019) were employed for this study. The FLEXPART-WRF

117 model was driven by mass-weighted wind fields and perturbation within the PBL calculated by WRF, which covers the

118 Northern Hemisphere with a 45-km horizontal resolution. The ERA5 global reanalysis (Hersbach et al., 2020) was used as the

119 initial and lateral boundary conditions of WRF, and the meteorological field of WRF was also nudged to ERA5 with e-folding

120 times of 3 hours and 12 hours for wind fields and temperature, respectively. Wet deposition is the major removal process for

121 BC, and the deposition process in FLEXPART version 10 (Grythe et al., 2017) was applied to the FLEXPART-WRF model

122 and was used in this study, with values of 10.0, 1.0, 0.9, and 0.1 employed as the collection efficiencies for wet deposition by

123 rain and snow and the activation efficiencies of cloud condensation nuclei (CCN) and ice nuclei (IN) (C_{rain}, C_{snow}, CCN$_{eff}$, and

124 IN$_{eff}$), respectively, which estimated by (Grythe et al., 2017) as the best parameters over several Arctic regions, i.e., Barrow,

Alert, and Zeppelin. The FLEXPART-WRF calculation was conducted every 6 hours from April 2016 to December 2020. For each simulation, 40000 particles were released at 0.5×0.5 degrees (horizontally) and from 0 to 200 m AGL (vertically) centred at the PFRR. The particles were tracked for 20 days at 6-hour intervals, and most simulated particles reached PFRR within approximately 10 days (Figure 4(c)). The primary output of the FLEXPART-WRF backward calculations was the potential emission sensitivity (PES), which expresses the residence time of particles at a given location and is used to characterize the transport pathways of the sampled air masses. The concentration of BC was estimated by multiplying PES and emissions based on a procedure reported by Sauvage et al. (2017). ECLIPSE (Evaluating the Climate and Air Quality Impacts of Short-Lived Pollutants) version 6b (Klimont et al., 2017) and GFED (Global Fire Emission Database) version 4.1 (Daily) (van der Werf et al., 2014) were used as the anthropogenic and biomass burning emissions, respectively. Note that the Chinese BC emissions from ECLIPSE version 6b with the monthly profile of version 5 are certified with downwind atmospheric BC observations (Kanaya et al., 2020), while other bottom-up inventories might result in a factor of ~2 overestimation. The PES fields were calculated with a horizontal resolution of 0.5×0.5 degrees. The contribution of particles within 100 m from the surface was considered for the calculation of PES for anthropogenic emissions. The plume height of the GFAS (Global Fire Assimilation System) (Di Giuseppe et al., 2017) was also used for the estimation of the injection height for biomass burning emissions. The fractional contribution of anthropogenic emissions was considered using eight sectors in the ECLIPSE emission, i.e., ship, gas flaring, waste incineration, transport, industry, energy, domestic, and agriculture, and the anthropogenic and biomass burning emissions were divided into eight regions, i.e., Europe, Central Asia, Russia, East Asia, Canada, Alaska, USA (excluding Alaska), and Others. The mean age of BC was also estimated by the mean lag time between release and observed time weighted by the amount of emission at each time period within the 20-day backward calculations.

2.4 Analysis of the effect of forest wildfire on the BC mass concentration at the PFRR

We characterized the observed BC/ΔCO ratios, which are known to be valuable indicators of emission sources and combustion conditions (Kondo et al., 2011b; Pan et al., 2017; Selimovic et al., 2019), in terms of fire radiative power (FRP), which accounts for forest wildfire intensity. To do this, we compared the BC/ΔCO ratio in high BC mass concentration cases (see section 3.4) observed between June and September (406 hours in total) and FRP observed by the Visible Infrared Imaging Radiometer Suite (VIIR) on the Suomi NPP satellite. Airmasses were traced for 4 days at the most using the Hybrid Single-Particle Lagrangian Integrated Trajectory model (HYSPLIT; (Stein et al., 2015)) with GDAS1 meteorological datasets (3 h archived $1° \times 1°$ Global Data Assimilation System) from the National Centers for Environmental Prediction (http://ready.arl.noaa.gov/gdas1.php; accessed on 2 November 2023). The calculation started from 500 m AGL at the PFRR site, and fire spots were searched along with the trajectories.

155 The BC/ΔCO ratio is also affected by atmospheric processes (Kanaya et al., 2016; Choi et al., 2020), as only BC is lost via

156 wet removal processes. To extract observation results that were not affected by wet removal processes, we used accumulated

157 precipitation along the trajectory (APT) as an indicator of wet removal processes. Previous studies showed that the BC/ΔCO

158 ratio can be changed when APT is larger than 1 mm (Choi et al., 2020; Kanaya et al., 2016; Kondo et al., 2011b). Therefore,

159 the duration for the accumulation of fire spots was shortened when APT reached 1 mm or when the trajectory reached ground

160 level. Rectangles were defined with ±0.5° in the longitudinal direction and ±0.25° in the latitudinal direction centring around

161 hourly air mass positions. Then, the FRP and the number of hot spots were accumulated for individual rectangles over the

162 duration of the trajectories. Finally, the total accumulated FRP (∑FRP) was divided by the detected total spot number to yield

163 an index describing the conditions of fires affecting the observed airmasses. As hot spot datasets, VIIRS 375 m

164 (VNP14IMGTML_NRT) archived datasets (countries were "United States" and "Canada") from the Fire Information for

165 Resource Management System (FIRMS) website (https://earthdata.nasa.gov/firms; accessed on 2 November 2023) were used

166 in this study. The selected confidence levels were 'nominal' or 'high', and the selected type attributed to thermal anomalies

167 was 'presumed vegetation fire'. In addition, we used FRP values greater than 0.3 MW for each hot spot because hot spots

168 smaller than 0.3 MW included outliers (Figure S2). Only hot spots that were observed within the previous 24 hours were

169 considered. Through this procedure (hereafter, we simply use 'back trajectory'), forest wildfires in Alaska and western Canada

170 (∑FRP>0) were detected in 184 cases of hourly BC observation results. Note that we also confirmed that no back trajectories

171 could suggest forest wildfires in other seasons.

172

173 **3 Results and discussion**

174 **3.1 Time series of observed BC and CO concentrations**

175 The time series of BC mass concentration and CO mixing ratio are shown in Figure 2, and those of annual median, 10th, and

176 90th percentile values are summarized in Table 1. The median hourly BC mass concentration and 10th and 90th percentile

177 values throughout the observation period were 13, 3, and 56 ng m^{-3}, respectively. No clear increase in annual median BC mass

178 concentration was observed (Table 1). Observed median BC mass concentrations were the same level as previous reports at

179 Utqiagvik (Barrow) (12 ng m^{-3}), which showed BC mass concentration over the long term using the same instrument

180 (BCM3130) employed in this study (Sinha et al., 2017; Mori et al., 2020). Abrupt peaks (up to 5540 ng m^{-3}) were occasionally

181 observed during summer at PFRR, but these peaks were not observed at Utqiagvik. On the other hand, increases in BC mass

182 concentrations were reported in Utqiagvik between January and March, while not in PFRR. These different variations may be

183 attributed to the topological separation by the Brooks mountain range and to the polar dome structure (Quinn et al., 2007;

184 Sharma et al., 2013).

185   The median, 10th, and 90th percentiles of hourly CO mixing ratios throughout the observation period were 124.7, 99.0, and

186   148.2 ppb, respectively. Similar to BC, increases in the annual median CO mixing ratio were not observed, but contrary to the

187   BC mass concentration, the CO mixing ratio showed clear seasonal variation, high in spring (between February and April,

188   143.5 ppb in the median) and low in summer (July and August, 103.3 ppb in the median) (Figure 2(b)). These observed CO

189   mixing ratios and seasonal variations were consistent with previous studies that reported the CO mixing ratio at the PFRR

190   (Kasai et al., 2005; Yurganov et al., 1998). In summer, CO peaks coincident with BC mass concentration were found,

191   suggesting a common emission source for both BC and CO.

192

193   Table 1. Annual summary of the observed hourly BC mass concentration and CO mixing ratio at the PFRR.

Year	BC (ng m^{-3})			CO (ppb)		
	Median	10th percentile	90th percentile	Median	10th percentile	90th percentile
2016[a]	11	2	49	109.7	93.1	130.3
2017	15	3	65	128.2	100.5	148.8
2018	14	3	53	118.2	93.3	149.4
2019	15	3	63	128.4	113.1	150.8
2020	13	3	50	131.3	107.5	150.6

194   [a] Observations started on 28 April 2016.

195
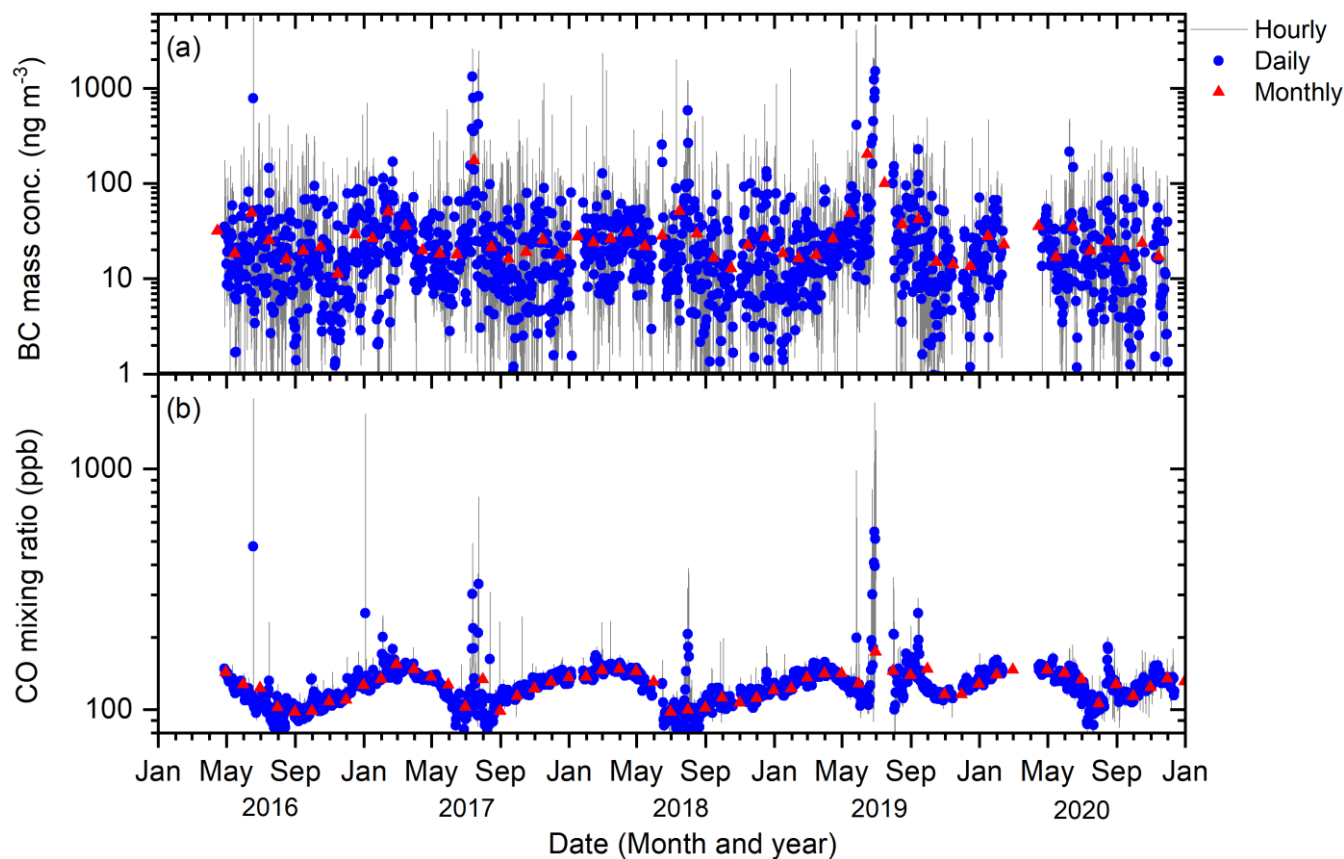
196
197   Figure 2. Time series of (a) BC mass concentration and (b) CO mixing ratio. Grey lines, blue points, and red triangles show
198   hourly, daily, and monthly averages, respectively.

199

3.2 Comparisons with other observation sites

We compared the BC observation results from the PFRR to those from other Alaskan sites (Table 2 and Figure S3), i.e., Trapper Creek (TRCR), Denali (DENA), and Toolik Lake Field Station (TOOL), using datasets for 24-hour filter samples collected every three days. The datasets were from the thermal/optical reflectance method at DENA, TRCR, and TOOL (http://views.cira.colostate.edu/fed/QueryWizard/; accessed on 2 November 2023). A systematic bias might be present in terms of the methods used, but it is most likely within a factor of 2 from the actual conditions based on comparisons with recent data at various sites (Miyazaki et al., 2008; Kondo et al., 2009; Kanaya et al., 2008; Kondo et al., 2011a; Ohata et al., 2021; Sinha et al., 2017). For the BC mass concentration observed at TRCR, DENA, and TOOL, datasets flagged V0 (valid value) were selected.

The BC mass concentration peaks were nearly coincided for the PFRR, DENA, TRCR, and TOOL (Figure S3). The median and maximum daily BC mass concentrations observed at each site are summarized in Table 2. The median BC mass concentrations at DENA, TRCR, and TOOL were larger than those at the PFRR by 6–19 ng m^{-3} (Table 2), but the significance of the difference is unclear considering methodological differences and associated uncertainties (precision). Here, the uncertainties of the thermal/optical reflectance method varied between 12 and 14 ng m^{-3} in median values during the whole observation period. Note that our BC observation, which had a better LOD (2 ng m^{-3}) and higher temporal resolution (1 hour), could provide more reliable data in this low range. On the other hand, the maximum BC mass concentrations were higher at the PFRR within the period with common BC peaks than at TRCR and TOOL but similar at DENA (Table 2). This indicates that strong BC emissions in central Alaska were better captured at the PFRR than at other observation sites because PFRR is the only BC-measuring site located in the central interior of Alaska and is surrounded by forest wildfire occurring regions while other BC observation sites are located on the edge or outside of interior Alaska. We will discuss source and emission ratio characterization in Sections 3.4 and 3.5 by fully utilizing the superior temporal resolution and accuracy of our observations.

Table 2. Summary of site locations and measurement results at PFRR (this study), TRCR, DENA, and TOOL.

				Daily BC mass concentration (ng m^{-3})	
Site	Latitude (°N)	Longitude (°W)	Altitude (m a.s.l)	Median	Maximum
PFRR[a]	65.12	147.43	500	18	920
TRCR	62.32	150.32	155	37	570
DENA	63.73	148.97	658	24	1044

TOOL[b]	68.64	149.61	740	28	643

224   [a] Data were selected from the same date at PFRR, TRCR, and DENA.

225   [b] Observations started on 13 November 2018.

226

227   **3.3 Comparison of observation and model simulations and possible BC sources**

228   Figure 3(a) shows a time series of 6-hour averages of the observation data and 6-hourly BC mass concentrations estimated by

229   FLEXPART-WRF simulations. FLEXPART-WRF could capture the high BC mass concentration peaks (Figure 3(a)) with a

230   correlation coefficient of 0.7 (Figure S4). The median of the simulated/observed ratio (observation data > LOD in this case)

231   was 1.0 for the whole observation period, indicating good agreement between the model simulation and observations.

232   The source region and source sector contributions derived from the FLEXPART-WRF simulation are shown in Figure 3(b)

233   and (c). The BC source sectors and regions varied clearly according to the season (Figure 3(b) and (c)). In the warm season

234   (between May and September), the possible BC source regions were Russia (3.6–74% in the 10–90 percentile) and Alaska

235   (12–85% in the 10–90 percentile) and sometimes Canada (1.0–21% in the 10–90 percentile) (Figure 3(b)), and the possible

236   source sector was estimated to be biomass burning (8.1–88% in the 10–90 percentile) (Figure 3(c)), especially when BC mass

237   concentration was high, suggesting that BC contributions from biomass burning that occurred in Russia, Alaska, and Canada

238   are dominant for BC mass concentrations at the PFRR. As snow cover disappears from the ground and the atmospheric

239   conditions become drier, forest wildfires caused by lightning increase in these warm seasons (Reap, 1991; Kaplan and Lau,

240   2021), resulting in increases in BC emissions from biomass burning (AMAP, 2021). We will focus on these high BC mass

241   concentration cases from Alaska and discuss the relationship between forest wildfire intensity and the BC/ΔCO ratio in the

242   following section.

243   On the other hand, in the cold seasons (between October and April), the domestic (24–48% in the 10–90 percentile) and

244   transport sectors (25–48% in the 10–90 percentile) were estimated to be possible dominant BC source sectors (Figure 3(c)).

245   The dominant source region was Alaska (19–88% in the 10–90 percentile), and occasionally, Russia (0.89–31% in the 10–90

246   percentile) and East Asia (1.2–41% in the 10–90 percentile) contributed to the BC mass concentration in PFRR(Figure 3(b)).

247
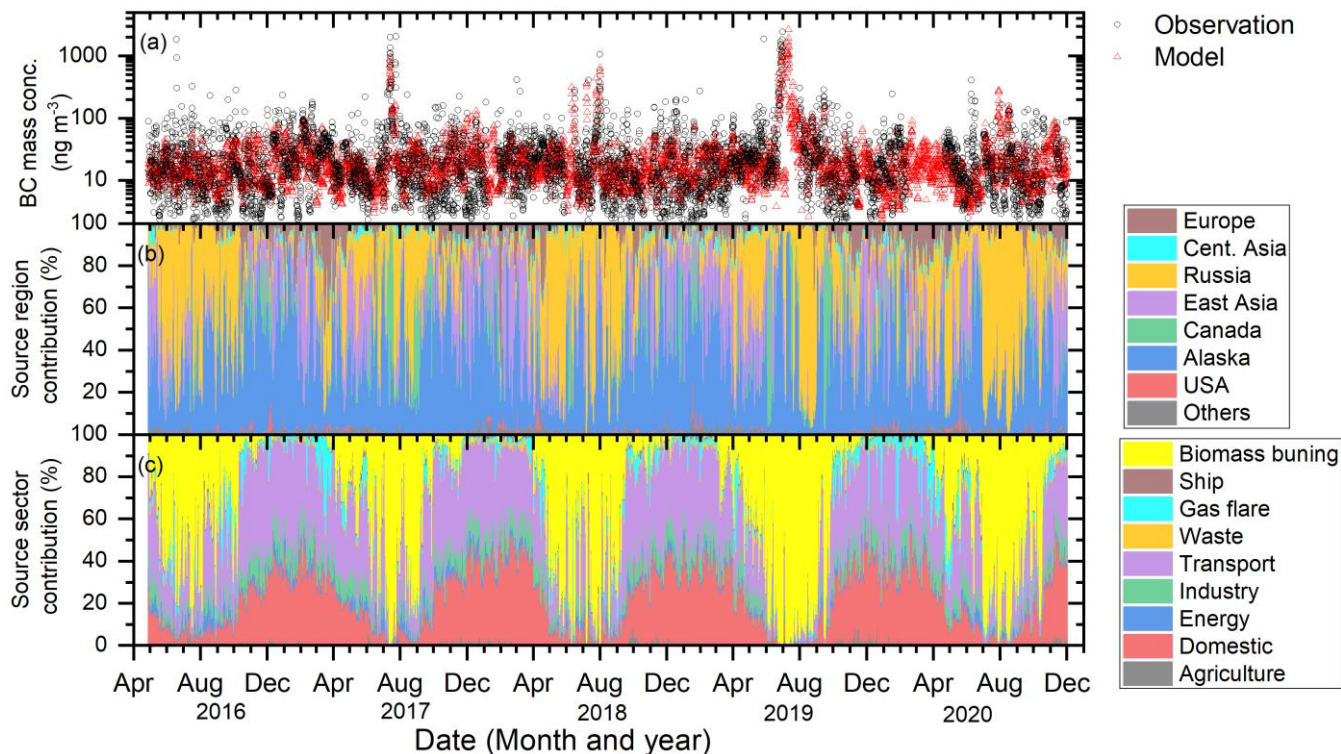
Figure 3. Time series of (a) BC mass concentrations from observations at the PFRR (6-hour average) and FLEXPART-WRF estimates (6 hours). Black circles and red triangles show the observed and simulated BC mass concentrations, respectively. Time series of simulated 6-hourly (b) contributions from BC source regions and (c) contributions from BC source sectors estimated by FLEXPART-WRF simulation. Individual colours show the source regions and sectors.

3.4 Biomass burning contribution for high BC concentration cases

Hereafter, we focus on high BC mass concentration cases at the PFRR (647 hours in total), which were selected with the 98 percentile value (171 ng m^{-3}) as the threshold for the hourly BC mass concentration. The cumulative BC mass concentration observed in these high BC mass concentration cases accounted for 5.7–43% of the annual BC mass concentration, although the duration of these periods was very short (17–187 hours in a year). Most of these high BC concentration cases (approximately 90%) were observed in warm seasons (between June and September) and were related to forest wildfires in Alaska. The median CO mixing ratio for the high BC concentration cases (174.7 ppb) was also higher than that in other periods (124.7 ppb), suggesting that both BC and CO were emitted from forest wildfires (see Section 3.3).

262 The normalized frequency distribution of the BC/ΔCO ratio for the high BC mass concentration cases is shown in Figure 4(a).

263 The median, 10th, and 90th percentile values of the BC/ΔCO ratio during these periods were 4.7, 1.8, and 18 ng m^{-3} ppb^{-1},

264 respectively. These observed BC/ΔCO ratios in the high BC mass concentration cases were in the same range or sometimes

265 higher than those in previous studies that reported the BC/ΔCO ratios from boreal forest wildfire emissions in Canada (Kondo

266 et al., 2011b) and Siberia (Paris et al., 2009; Chi et al., 2013; Vasileva et al., 2017).

267 The medians of the contributions of biomass burning and the mean age of BC estimated by the FLEXPART-WRF simulation

268 in these high BC mass concentration cases were higher and shorter (95.5% and 2.6 days) than those in other periods (7.6% and

269 6.9 days) (Figure 4(b) and (c)), indicating a strong contribution of BC from neighbouring forest wildfires (Figure S5). We also

270 calculated the 6-hourly mass-weighted biomass burning contributions from individual source regions (6 categories based on

271 Figure 3(b), Central Asia and Europe are included in Others) to the BC mass concentrations at the PFRR (Figure 5). As a result,

272 we found that large peaks, such as those observed between June and August in 2017, 2018, and 2019, coincided well with the

273 peaks of BC contributions mostly from forest wildfires in Alaska (Figure S5). BC from forest wildfires that occurred in western

274 Canada also affected the BC concentration at PFRR (Figure S6) but to a lesser frequency. Russia was also estimated as an

275 effective BC source region (Figure 3), but BC concentration did not exceed 0.1 µg m^{-3} in most cases (Figure 5). These results

276 confirmed that the observed high BC mass concentration cases were primarily affected by local forest wildfires in Alaska.

277 These peaks were widely observed in Alaska (Section 3.2) and imply a large impact of local forest wildfires on BC mass

278 concentration in this region. However, when these high BC mass concentration cases were selected, the median of the

279 simulated/observed ratio was 0.30, indicating underestimation in the model simulation (possibly due to insufficient spatial

280 resolution for neighbouring forest wildfires and difficulties in representing the vertical profiles of BC emissions) or/and in

281 emission inventories in the high BC mass concentration cases. Several studies have indicated that differences in different

282 inventories cause large uncertainties in model estimates of BC emissions, atmospheric concentrations, and radiative impacts,

283 especially in boreal North America (Carter et al., 2020; Pan et al., 2020). The impact of different inventories on model estimates

284 will be discussed in the future.

285

286
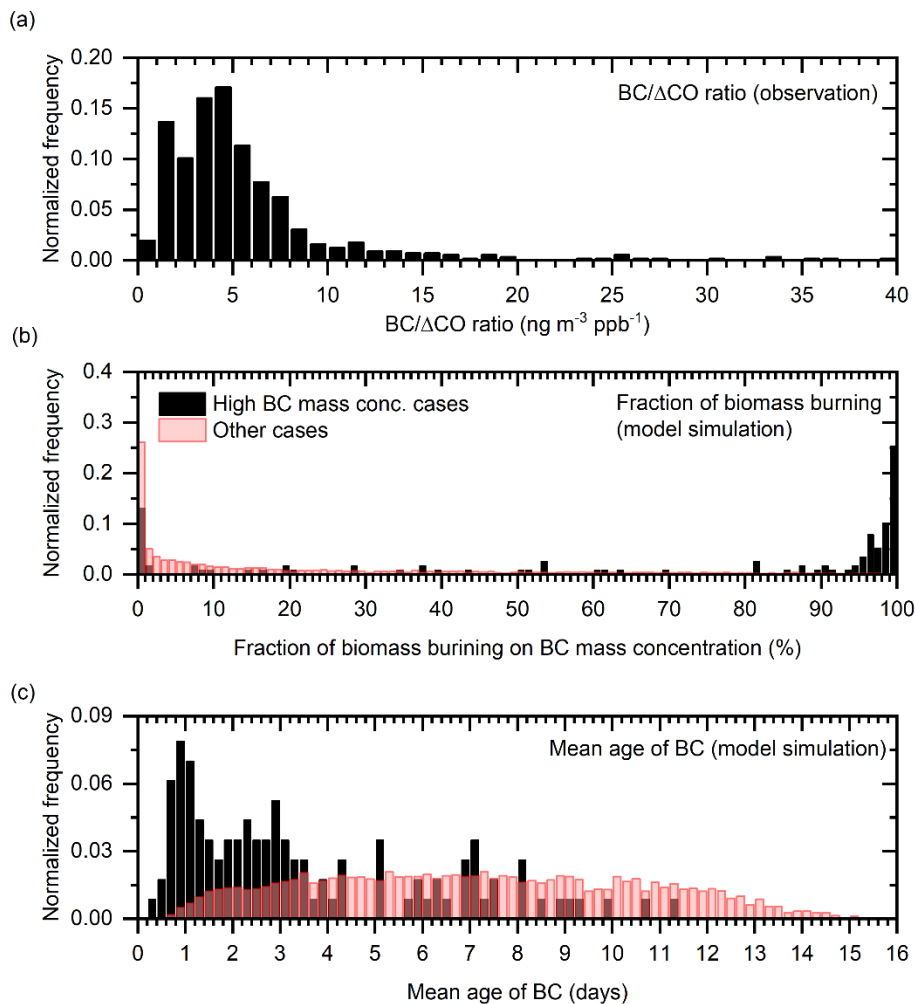
287
288 Figure 4. (a) A histogram of the observed BC/ΔCO ratio at the PFRR in high BC mass concentration cases. Histograms of the
289 (b) fractions of biomass burning on BC mass concentration and (c) mean age of BC simulated with the FLEXPART-WRF
290 model in high BC concentration cases and other cases. Black and red bars used in (b) and (c) indicate high BC concentration
291 cases and other cases, respectively. Hourly results are shown for the observed BC/ΔCO ratio (a), and 6-hourly results are
292 shown for the FLEXPART-WRF simulation ((b) and (c)).
293
294
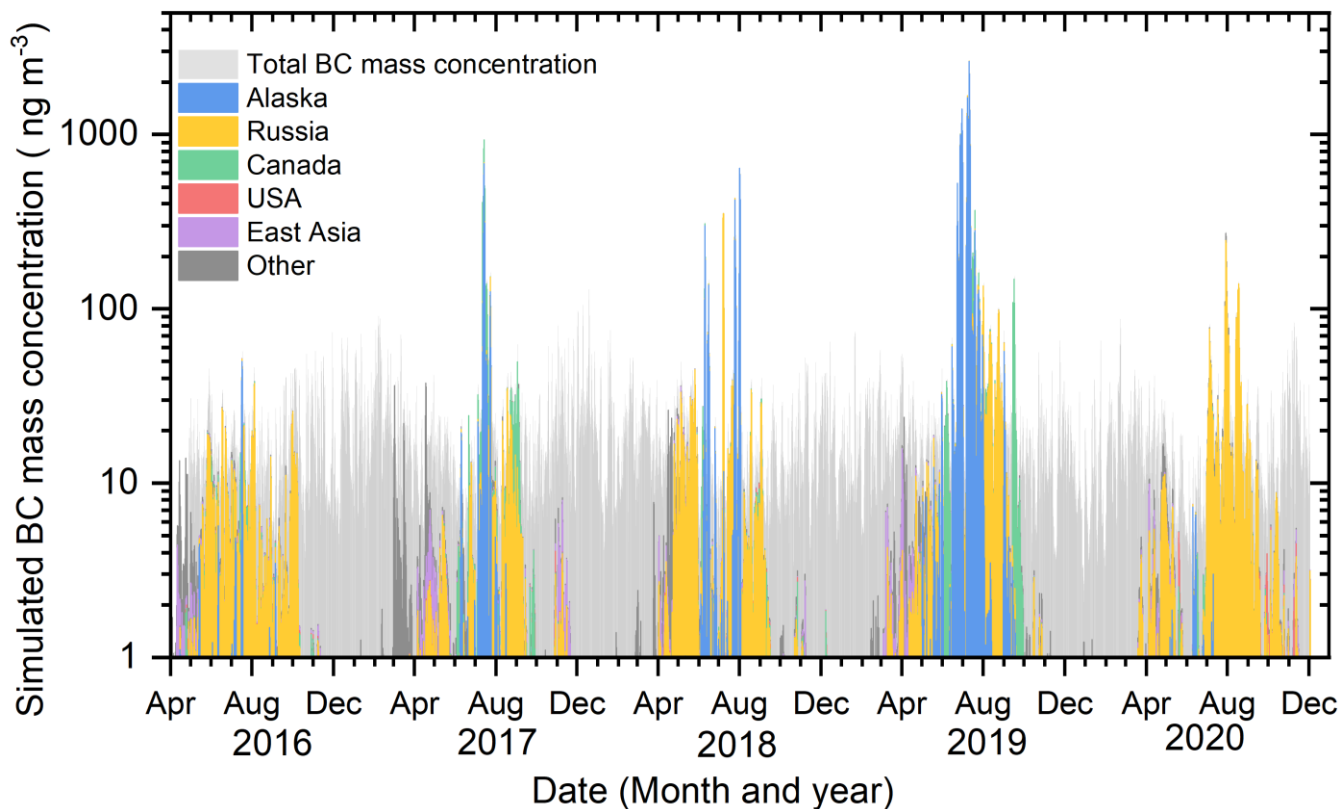
295

296 Figure 5. A stacked graph of the 6-hourly simulated BC mass concentration for all sources and mass-weighted biomass burning

297 contributions for BC mass concentration at the PFRR estimated with FLEXPART-WRF simulations. Grey bars indicate the

298 total BC mass concentration for all sources, and the colours show the individual source regions.

299

300 **3.5 Relationship between the BC/ΔCO ratio and FRP**

301 In the previous section, we showed that most high BC mass concentration cases were related to forest wildfires in Alaska.

302 Increases in biomass-burning-derived BC/ΔCO ratios with combustion efficiency were suggested from an observational study

303 on boreal forest wildfire (Kondo et al., 2011b) and from laboratory-scale burning experiments of crop residues (Pan et al.,

304 2017); however, in-depth studies examining variabilities in BC/ΔCO ratios based on long-term, near-forest observations have

305 not been conducted. To consider the possibility that combustion conditions (flaming and smouldering) primarily control the

306 BC/ΔCO ratio, we are going to investigate the relationship between the BC/ΔCO ratio and forest wildfire intensity in this

307 section.

308 We found a positive correlation (r = 0.44, p < 0.0001, n = 184) between the BC/ΔCO ratio and $\sum$FRP/point values (Figure 6).

309 This positive correlation between the BC/ΔCO ratio and ΣFRP/point values, represented for the first time to our knowledge,

310 is qualitatively consistent with previous studies that showed that high combustion efficiency (larger than 0.9 in modified

311 combustion efficiency value (MCE)) increased BC/ΔCO ratios (Selimovic et al., 2019; Kondo et al., 2011b; Pan et al., 2017),

312 which is related to the fact that the BC production process is mostly related to the flaming process (high MCE), while that of

313 CO is related to the smouldering process (low MCE). For example, Pan et al. (2017) measured BC, CO, and CO_2 from biomass

314 burning in small-scale combustion experiments. In their experiment, dry and wet wheat straw samples and dry rapeseed plant

315 samples were burned, and the time evolution of BC/ΔCO ratio and MCE were observed. They reported that BC is mostly

316 produced during the flaming process, and the evolution of the BC/ΔCO ratio which depends on the combustion stage could be

317 confirmed (13.9±10.1 ng m^{-3} ppbv^{-1} for MCE larger than 0.95 cases, and less than 7.1 ng m^{-3} ppbv^{-1} for MCE smaller than

318 0.96 cases). Although these BC/ΔCO ratios are larger than our observed BC/ΔCO ratio, differences in fuels might be a possible

319 reason. Selimovic et al. (2018) also burned some types of fuels, including coniferous trees, in a large indoor combustion facility

320 and measured BC, CO, and CO_2 with various other chemical species. They reported a high BC/ΔCO ratio (13.8 ng m^{-3} ppbv^{-1}

321 on average) and a low BC/ΔCO ratio (4.7 ng m^{-3} ppbv^{-1} on average) in the condition of flaming-dominated and smouldering-

322 dominated, respectively, in the same range as our observed values. Moreover, Chakrabarty et al. (2016) tested Alaskan peat

323 and Siberian peat in the combustion chamber under smouldering conditions, and low BC/ΔCO ratios (1.2–2.6 ng m^{-3} ppbv^{-1})

324 were reported. The positive relationship between the BC/ΔCO ratio and MCE is also observed in the field measurements

325 (Kondo et al., 2011b; Selimovic et al., 2019). Although MCE and FRP are different parameters, both parameters indicate

326 combustion conditions and have a strong correlation (Wiggins et al., 2020). Therefore, for the first time, we report a positive

327 correlation between the BC/ΔCO ratio and FRP as a combustion condition indicator. The wide range of BC/ΔCO ratios reported

328 from boreal forest wildfires, from 1.7–3.4 ng m^{-3} ppb^{-1} (Kondo et al., 2011b) to 6.1–6.3 ng m^{-3} ppb^{-1} (Vasileva et al., 2017),

329 could be better explained when the index introduced here (ΣFRP/point) is considered. This relationship should be taken into

330 account when constructing future emission inventories from boreal forest wildfires.

331 A positive correlation was found after optimizing the spatial window size (±0.5° in the longitudinal direction and ±0.25° in

332 the latitudinal direction), in which hot spots were taken into account for each hour along the trajectory (from -96 to 0 hours),

333 and the associated time window was used to determine coincident fires that affected the observations (from -24 to 0 hours).

334 Based on the spatial resolution of GDAS1 (1° × 1°), we set our initial windows as ±0.5° for latitude and longitude. However,

335 PFRR is in a high latitude and the geometrical length of latitude is approximately 2 times longer than that of longitude. For

336 this reason, we defined latitudinal width as ±0.25° finally. Although we tested finer window size cases, a similar positive trend

337 was confirmed. The remaining scatter might have arisen from differences in the detection of hot spots in the presence of clouds

338 (Li et al., 2018). To overcome shortcomings in hot spot detection, improvements in the frequency of hot spot scanning should

339 be made, for example, via the use of MODerate Resolution Imaging Spectroradiometer (MODIS) combined with VIIRS

340 observations; it should be noted, however, that there is abias in FRP observations between MODIS and VIIRS, especially for

341 boreal forests (Li et al., 2018). Improvements in the accuracy and consistency of FRP analysis between multiple satellite

342 observations can facilitate a more in-depth understanding of the relationship between FRP and the BC/ΔCO ratio.

343 The simulated/observed ratios in high BC mass concentration cases were low (0.30, Section 3.3), contrary to the good

344 agreement observed in overall cases (1.0, Section 3.3). The BC/ΔCO ratios in commonly used emission inventories are 4.9 ng

345 m^{-3} ppb^{-1} for GFED4s (van der Werf et al., 2017) and 4.4 ng m^{-3} ppb^{-1} for Andreae (2019) and are in a range similar to that of

346 our median BC/ΔCO ratio. However, our observed BC/ΔCO ratios in high BC concentration cases for forest wildfires had a

347 broad range between 1.7 and 7.3 ng m^{-3} ppb^{-1} at the 10 and 90 percentiles (median was 4.2 ng m^{-3} ppb^{-1}), respectively, related

348 to the $\sum$FRP/point values. This implies that the BC emission factors from biomass burning could vary depending on the FRP.

349 Although several previous inventory studies used FRP for the estimation of activity data (Carter et al., 2020), namely, fuel

350 burned or burned area, no inventories included the evolution of the emission factors of BC and/or CO. Our findings suggest

351 the potential for improving BC emission inventories and/or emission factors by using FRP. In addition, BC emission estimation

352 using satellites would be improved by using our results. CO emissions estimated by satellite observations are sometimes used

353 to estimate other pollutant emissions from forest fires using emission ratios derived from in situ measurements (Zheng et al.,

354 2023). As its extension, BC emissions could be estimated, regarding our quantified BC/ΔCO ratios and their evolutions with

355 FRP directly as the emission ratio of BC to CO. The frequency of boreal forest fires may increase in the future (Box et al.,

356 2019; Hu et al., 2015); as a result, their impact on climate and air quality might become more severe in Alaska and the Arctic

357 (Kim et al., 2005; Schmale et al., 2018; Stohl et al., 2006). Our long-term observations of BC and CO at an hourly temporal

358 resolution in the interior of Alaska provide unique information to test model simulations and emission inventories relevant to

359 the climate and air quality of the Arctic.

360

$$y = 0.11(\pm 0.02)\, x + 2.5\, (\pm 0.22)$$
$$r = 0.44,\ p < 0.0001,\ n = 184$$
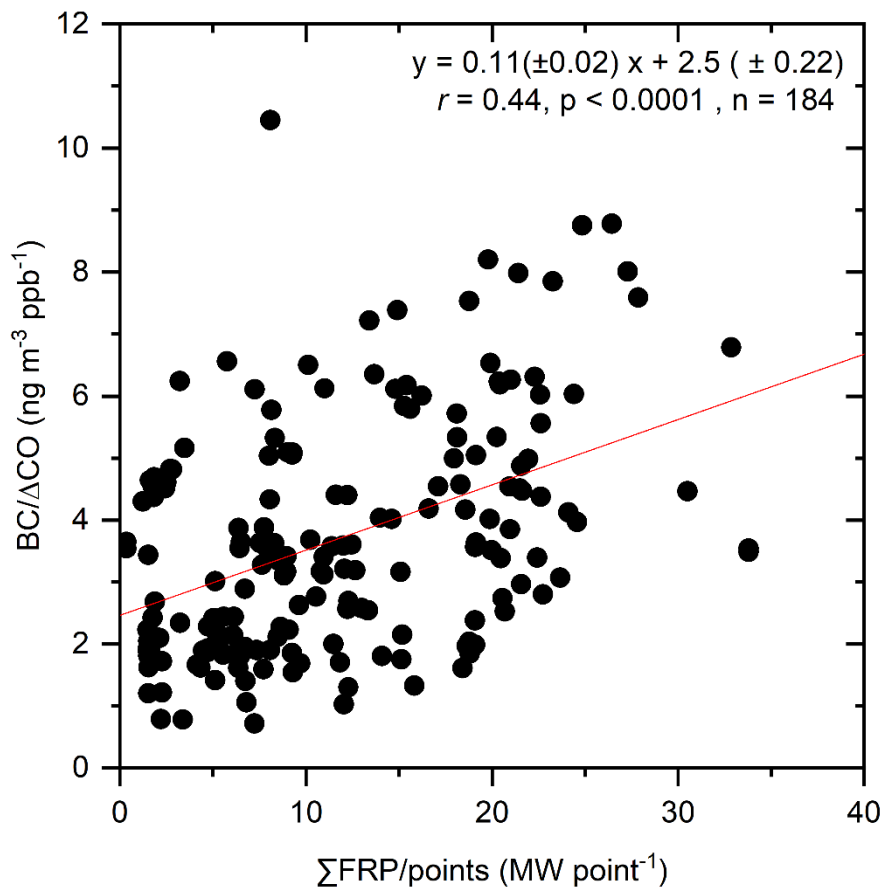
361

362 Figure 6. Correlation between the BC/ΔCO ratio in the high BC mass concentration cases observed at the PFRR and

363 $\sum$FRP/point values. The linear regression curve is shown by a red line.

364

4 Conclusion

366 We showed key features of the BC and CO concentrations observed at the PFRR in interior Alaska since 2016 in this paper.

367 The annual medians of the BC mass concentration and CO mixing ratio were 11–15 ng m^{-3} and 109.7–131.3 ppb, respectively.

368 Large and short-term increases in BC mass concentrations were sometimes observed between June and September. A clear

369 seasonal variation was observed in the CO mixing ratio, which was high in spring (between February and April, 143.5 ppb in

370 the median) and low in summer (July and August, 103.3 ppb in the median). The CO mixing ratio coincided with the high BC

371 mass concentration peaks, suggesting a strong contribution from forest wildfires to BC and CO concentrations.

372 The BC mass concentrations observed at other sites in Alaska, i.e., DENA, TRCR, and TOOL, were compared with our results.

373 The annual median BC mass concentrations at the PFRR were lower than those at TRCR, DENA, and TOOL, but coinciding

374 BC mass concentration peaks were found at these observation sites. In these high BC mass concentration cases, BC mass

375 concentrations at the PFRR were larger than those at TRCR and TOOL but similar at DENA, indicating that strong BC

376 emissions from forest wildfires occurred in interior Alaska and affected broad areas in Alaska.

377 The dominance of forest wildfires in Alaska as a major cause of high BC mass concentration was also supported by the model

378 simulations. We simulated BC mass concentration using the FLEXPART-WRF model and compared the simulations with the

379 observation results. The model simulation could capture observational results (r = 0.70) in which the median

380 simulated/observed ratio was 1.0. The estimated BC source sectors and regions were biomass burning from Russia, Alaska,

381 and sometimes Canada between May and September, while those for other periods were domestic sources and transport and

382 were mainly from Alaska.

383 When we focused on high BC mass concentration cases (greater than 98 percentile values), we found that forest wildfires

384 occurring in Alaska were the dominant source of BC in those cases from the model simulation results. The mean ages of BC

385 and biomass burning contributions in these high BC mass concentration cases estimated by FLEXPART-WRF were 2.6 days

386 and 95.5%, respectively, relatively shorter and higher than those in other cases (6.9 days and 7.6%, respectively). The peaks

387 of the calculated biomass burning contributions from Alaska to BC mass concentrations at the PFRR coincided well with

388 observed and simulated peaks in high BC mass concentration cases, suggesting that the forest wildfires that occurred around

389 the PFRR are important.

390 The median observed BC/ΔCO ratio in high BC mass concentration cases related to forest wildfires was 4.2 ng m^{-3} ppb^{-1} and

391 was in the same range as that in previous studies reporting the BC/ΔCO ratio of boreal forest wildfire emissions. Finally, we

392 tracked airmass origin for 4 days using the HYSPLIT model with FRP satellite observations in these cases and investigated

393 the relationship between the observed BC/ΔCO ratio and FRP, which was normalized by the number of hot spots (points)

394 observed by VIIRS. A positive correlation was found between these parameters (r = 0.44). For the first time, the properties of

395 the BC/ΔCO ratio from boreal forest wildfires were systematically characterized in terms of FRP, suggesting the potential to

396 improve emission inventories and/or emission factors by using FRP.

397

Data availability

399 The BC and CO observation results are available online (https://ads.nipr.ac.jp/dataset/A20241101-003). We used public data

400 for BC observation results at Denali, Trapper Creek, and Toolik Lake Field Station

401 (http://views.cira.colostate.edu/fed/QueryWizard/).

402

Supplement

The supplement related to this article is available online at https://doi.org/xxxxxxxx.

Author contributions

TK, FT, CZ, YKi, and YKa conducted and recorded observations for BC and CO at the PFRR site. MT conducted the FLEXPART-WRF model simulations. YKi assisted in the fieldwork at the PFRR site. TK, FT, MP, and YKa summarized the observation results, and TK wrote the first draft with MT. All authors contributed to the discussion and writing of the manuscript.

Competing interests

At least one of the (co-)authors is a member of the editorial board of Atmospheric Chemistry and Physics.

Acknowledgement

The authors acknowledge technical support from Dr. Takuma Miyakawa, a researcher at JAMSTEC and help with field work from Dr. Hideki Kobayashi, a researcher at JAMSTEC. The authors also thank all the supporting members at JAMSTEC. The authors thank NOAA ARL for providing the CO aircraft observation data, HYSPLIT model, and GDAS1 meteorological data. We also thank the IMPROVE network. IMPROVE is a collaborative association of state, tribal, and federal agencies and international partners. The US Environmental Protection Agency is the primary funding source, with contracting and research support from the National Park Service. The Air Quality Group at the University of California, Davis, was the central analytical laboratory, and carbon analysis was carried out by the Desert Research Institute. We also thank the anonymous reviewers for their precise and valuable comments that greatly improved the paper.

Financial support

This work was funded by the Arctic Challenge for Sustainability II (ArCS II), Program Grant Number JPMXD1420318865, the Arctic Challenge for Sustainability (ArCS), Program Grant Number JPMXD1300000000, and a National Research Foundation of Korea Grant from the Korean Government (MSIT; the Ministry of Science and ICT, NRF-2021M1A5A1065425) (KOPRI-PN24011).

References

Aizawa, T., Ishii, M., Oshima, N., Yukimoto, S., and Hasumi, H.: Arctic warming and associated sea ice reduction in the early 20th century induced by natural forcings in MRI-ESM2.0 climate simulations and multimodel analyses, Geophys. Res. Lett., 48, https://doi.org/10.1029/2020gl092336, 2021.

AMAP: The Impact of Black Carbon on Arctic Climate, Arctic Monitoring and Assessment Programme (AMAP), 2011.

AMAP: AMAP Assessment 2021:Impacts of Short-lived Climate Forcers on Arctic Climate, Air Quality, and Human Health, Arctic Monitoring and Assessment Programme (AMAP), 2021.

Aoki, T., Kuchiki, K., Niwano, M., Kodama, Y., Hosaka, M., and Tanaka, T.: Physically based snow albedo model for calculating broadband albedos and the solar heating profile in snowpack for general circulation models, J. Geophys. Res., 116, https://doi.org/10.1029/2010jd015507, 2011.

Bian, H., Colarco, P. R., Chin, M., Chen, G., Rodriguez, J. M., Liang, Q., Blake, D., Chu, D. A., Silva, A. da, Darmenov, A. S., and Others: Source attributions of pollution to the Western Arctic during the NASA ARCTAS field campaign, Atmos. Chem. Phys., 13, 4707–4721, https://doi.org/10.5194/acp-17-15271-2017, 2013.

Bond, T. C., Anderson, T. L., and Campbell, D.: Calibration and Intercomparison of Filter-Based Measurements of Visible Light Absorption by Aerosols, Aerosol Sci. Technol., 30, 582–600, https://doi.org/10.1080/027868299304435, 1999.

Bond, T. C., Doherty, S. J., Fahey, D. W., Forster, P. M., Berntsen, T., DeAngelo, B. J., Flanner, M. G., Ghan, S., Kärcher, B., Koch, D., Kinne, S., Kondo, Y., Quinn, P. K., Sarofim, M. C., Schultz, M. G., Schulz, M., Venkataraman, C., Zhang, H., Zhang, S., Bellouin, N., Guttikunda, S. K., Hopke, P. K., Jacobson, M. Z., Kaiser, J. W., Klimont, Z., Lohmann, U., Schwarz, J. P., Shindell, D., Storelvmo, T., Warren, S. G., and Zender, C. S.: Bounding the role of black carbon in the climate system: A scientific assessment, J. Geophys. Res., 118, 5380–5552, https://doi.org/10.1002/jgrd.50171, 2013.

Bonfils, C. J. W., Santer, B. D., Fyfe, J. C., Marvel, K., Phillips, T. J., and Zimmerman, S. R. H.: Human influence on joint changes in temperature, rainfall and continental aridity, Nat. Clim. Chang., 10, 726–731, https://doi.org/10.1038/s41558-020-0821-1, 2020.

Box, J. E., Colgan, W. T., Christensen, T. R., Schmidt, N. M., Lund, M., Parmentier, F.-J. W., Brown, R., Bhatt, U. S., Euskirchen, E. S., Romanovsky, V. E., and Others: Key indicators of Arctic climate change: 1971--2017, Environ. Res. Lett., 14, 045010, https://doi.org/10.1088/1748-9326/aafc1b, 2019.

Bozem, H., Hoor, P., Kunkel, D., Köllner, F., Schneider, J., Herber, A., Schulz, H., Leaitch, W. R., Aliabadi, A. A., Willis, M. D., Burkart, J., and Abbatt, J. P. D.: Characterization of transport regimes and the polar dome during Arctic spring and summer using in situ aircraft measurements, Atmos. Chem. Phys., 19, 15049–15071, https://doi.org/10.5194/acp-19-15049-2019, 2019.

Brioude, J., Arnold, D., Stohl, A., Cassiani, M., Morton, D., Seibert, P., Angevine, W., Evan, S., Dingwell, A., Fast, J. D., Easter, R. C., Pisso, I., Burkhart, J., and Wotawa, G.: The Lagrangian particle dispersion model FLEXPART-WRF version 3.1, Geoscientific Model Development, 6, 1889–1904, https://doi.org/10.5194/gmd-6-1889-2013, 2013.

Buchhorn, M., Smets, B., Bertels, L., De Roo, B., Lesiv, M., Tsendbazar, N.-E., Herold, M., and Fritz, S.: Copernicus Global Land Service: Land Cover 100m: collection 3: epoch 2019: Globe, https://doi.org/10.5281/zenodo.3939050, 2020.

Cai, Z., You, Q., Wu, F., Chen, H. W., Chen, D., and Cohen, J.: Arctic Warming Revealed by Multiple CMIP6 Models: Evaluation of Historical Simulations and Quantification of Future Projection Uncertainties, J. Clim., 34, 4871–4892, https://doi.org/10.1175/JCLI-D-20-0791.1, 2021.

Carter, T. S., Heald, C. L., Jimenez, J. L., Campuzano-Jost, P., Kondo, Y., Moteki, N., Schwarz, J. P., Wiedinmyer, C., Darmenov, A. S., da Silva, A. M., and Kaiser, J. W.: How emissions uncertainty influences the distribution and radiative impacts of smoke from fires in North America, Atmos. Chem. Phys., 20, 2073–2097, https://doi.org/10.5194/acp-20-2073-2020, 2020.

Chakrabarty, R. K., Gyawali, M., Yatavelli, R. L. N., Pandey, A., Watts, A. C., Knue, J., Chen, L.-W. A., Pattison, R. R., Tsibart, A., Samburova, V., and Moosmüller, H.: Brown carbon aerosols from burning of boreal peatlands: microphysical properties, emission factors, and implications for direct radiative forcing, Atmos. Chem. Phys., 16, 3033–3040, https://doi.org/10.5194/acp-16-3033-2016, 2016.

Chi, X., Winderlich, J., Mayer, J.-C., Panov, A. V., Heimann, M., Birmili, W., Heintzenberg, J., Cheng, Y., and Andreae, M. O.: Long-term measurements of aerosol and carbon monoxide at the ZOTTO tall tower to characterize polluted and pristine air in the Siberian taiga, Atmos. Chem. Phys., 13, 12271–12298, https://doi.org/10.5194/acp-13-12271-2013, 2013.

Choi, Y., Kanaya, Y., Takigawa, M., Zhu, C., Park, S.-M., Matsuki, A., Sadanaga, Y., Kim, S.-W., Pan, X., and Pisso, I.: Investigation of the wet removal rate of black carbon in East Asia: Validation of a below-and in-cloud wet removal scheme in FLEXible PARTicle (FLEXPART) model v10. 4, Atmos. Chem. Phys., 20, 13655–13670, https://doi.org/10.5194/acp-20-13655-2020, 2020.

Cohen, J., Screen, J. A., Furtado, J. C., Barlow, M., Whittleston, D., Coumou, D., Francis, J., Dethloff, K., Entekhabi, D., Overland, J., and Jones, J.: Recent Arctic amplification and extreme mid-latitude weather, Nat. Geosci., 7, 627–637, https://doi.org/10.1038/ngeo2234, 2014.

Creamean, Maahn, and Boer: The influence of local oil exploration and regional wildfires on summer 2015 aerosol over the North Slope of Alaska, Atmos. Chem. Phys., https://doi.org/10.5194/acp-18-555-2018, 2018.

Di Giuseppe, F., Rémy, S., Pappenberger, F., and Wetterhall, F.: Combining fire radiative power observations with the fire weather index improves the estimation of fire emissions, Atmos. Chem. Phys. Discuss, https://doi.org/10.5194/acp-2017-790, 2017.

Duck, T. J., Firanski, B. J., Millet, D. B., Goldstein, A. H., Allan, J., Holzinger, R., Worsnop, D. R., White, A. B., Stohl, A., Dickinson, C. S., and van Donkelaar, A.: Transport of forest fire emissions from Alaska and the Yukon Territory to Nova Scotia during summer 2004, J. Geophys. Res., 112, https://doi.org/10.1029/2006jd007716, 2007.

Eck, T. F., Holben, B. N., Reid, J. S., Sinyuk, A., Hyer, E. J., O'Neill, N. T., Shaw, G. E., Vande Castle, J. R., Chapin, F. S., Dubovik, O., Smirnov, A., Vermote, E., Schafer, J. S., Giles, D., Slutsker, I., Sorokine, M., and Newcomb, W. W.: Optical properties of boreal region biomass burning aerosols in central Alaska and seasonal variation of aerosol optical depth at an Arctic coastal site, J. Geophys. Res., 114, https://doi.org/10.1029/2008jd010870, 2009.

Forster, C., Wandinger, U., Wotawa, G., James, P., Mattis, I., Althausen, D., Simmonds, P., O'Doherty, S., Jennings, S. G., Kleefeld, C., Schneider, J., Trickl, T., Kreipl, S., Jäger, H., and Stohl, A.: Transport of boreal forest fire emissions from Canada to Europe, J. Geophys. Res., 106, 22887–22906, https://doi.org/10.1029/2001jd900115, 2001.

Garrett, T. J., Brattström, S., and Sharma, S.: The role of scavenging in the seasonal transport of black carbon and sulfate to the Arctic, Geophys. Res. Lett., https://doi.org/10.1029/2011GL048221, 2011.

Gliß, J., Mortier, A., Schulz, M., Andrews, E., Balkanski, Y., Bauer, S. E., Benedictow, A. M. K., Bian, H., Checa-Garcia, R., Chin, M., and Others: AeroCom phase III multi-model evaluation of the aerosol life cycle and optical properties using ground-

505 and space-based remote sensing as well as surface in situ observations, Atmos. Chem. Phys., 21, 87–128,
506 https://doi.org/10.5194/acp-21-87-2021, 2021.

507 Grythe, H., Kristiansen, N. I., Groot Zwaaftink, C. D., Eckhardt, S., Ström, J., Tunved, P., Krejci, R., and Stohl, A.: A new
508 aerosol wet removal scheme for the Lagrangian particle model FLEXPART v10, Geoscientific Model Development, 10, 1447–
509 1466, https://doi.org/10.5194/gmd-10-1447-2017, 2017.

510 Halofsky, J. E., Peterson, D. L., and Harvey, B. J.: Changing wildfire, changing forests: the effects of climate change on fire
511 regimes and vegetation in the Pacific Northwest, USA, Fire Ecology, 16, 4, https://doi.org/10.1186/s42408-019-0062-8, 2020.

512 Hersbach, H., Bell, B., Berrisford, P., Hirahara, S., Horányi, A., Muñoz-Sabater, J., Nicolas, J., Peubey, C., Radu, R., Schepers,
513 D., Simmons, A., Soci, C., Abdalla, S., Abellan, X., Balsamo, G., Bechtold, P., Biavati, G., Bidlot, J., Bonavita, M., Chiara,
514 G., Dahlgren, P., Dee, D., Diamantakis, M., Dragani, R., Flemming, J., Forbes, R., Fuentes, M., Geer, A., Haimberger, L.,
515 Healy, S., Hogan, R. J., Hólm, E., Janisková, M., Keeley, S., Laloyaux, P., Lopez, P., Lupu, C., Radnoti, G., Rosnay, P.,
516 Rozum, I., Vamborg, F., Villaume, S., and Jean-Noël Thépaut: The ERA5 global reanalysis, Quart. J. Roy. Meteor. Soc., 146,
517 1999–2049, https://doi.org/10.1002/qj.3803, 2020.

518 Hu, F. S., Higuera, P. E., Duffy, P., Chipman, M. L., Rocha, A. V., Young, A. M., Kelly, R., and Dietze, M. C.: Arctic tundra
519 fires: natural variability and responses to climate change, Front. Ecol. Environ., 13, 369–377, https://doi.org/10.1890/150063,
520 2015.

521 Ikeda, K., Tanimoto, H., Sugita, T., Akiyoshi, H., Kanaya, Y., Zhu, C., and Taketani, F.: Tagged tracer simulations of black
522 carbon in the Arctic: transport, source contributions, and budget, Atmos. Chem. Phys., 17, 10515–10533,
523 https://doi.org/10.5194/acp-17-10515-2017, 2017.

524 IPCC: Climate change 2021: the physical science basis, edited by: Masson-Delmotte, V., Zhai, P., Pirani, A., Connors, S. L.,
525 Péan, C., Berger, S., Caud, N., Chen, Y., Goldfarb, L., Gomis, M. I., and Others, Cambridge University Press Cambridge, UK,
526 2021.

527 Kanaya, Y., Komazaki, Y., Pochanart, P., Liu, Y., Akimoto, H., Gao, J., Wang, T., and Wang, Z.: Mass concentrations of
528 black carbon measured by four instruments in the middle of Central East China in June 2006, Atmos. Chem. Phys., 8, 7637–
529 7649, https://doi.org/10.5194/acp-8-7637-2008, 2008.

530 Kanaya, Y., Pan, X., Miyakawa, T., Komazaki, Y., Taketani, F., Uno, I., and Kondo, Y.: Long-term observations of black
531 carbon mass concentrations at Fukue Island, western Japan, during 2009--2015: constraining wet removal rates and emission
532 strengths from East Asia, Atmos. Chem. Phys., 16, 10689–10705, https://doi.org/10.5194/acp-16-10689-2016, 2016.

533 Kanaya, Y., Yamaji, K., and Miyakawa, T.: Rapid reduction in black carbon emissions from China: evidence from 2009–2019
534 observations on Fukue Island, Japan, Atmos. Chem. Phys., https://doi.org/10.5194/acp-20-6339-2020, 2020.

535 Kaplan, J. O. and Lau, K. H.-K.: The WGLC global gridded lightning climatology and time series, Earth Syst. Sci. Data, 13,
536 3219–3237, https://doi.org/10.5194/essd-13-3219-2021, 2021.

537 Kasai, Y. J., Koshiro, T., Endo, M., Jones, N. B., and Murayama, Y.: Ground-based measurement of strato–mesospheric CO
538 by a FTIR spectrometer over Poker Flat, Alaska, Adv. Space Res., 35, 2024–2030, https://doi.org/10.1016/j.asr.2005.04.099,
539 2005.

540 Kim, Y., Hatsushika, H., Muskett, R. R., and Yamazaki, K.: Possible effect of boreal wildfire soot on Arctic sea ice and Alaska
541 glaciers, Atmos. Environ., 39, 3513–3520, https://doi.org/10.1016/j.atmosenv.2005.02.050, 2005.

Klimont, Z., Kupiainen, K., Heyes, C., Purohit, P., Cofala, J., Rafaj, P., Borken-Kleefeld, J., and Schöpp, W.: Global anthropogenic emissions of particulate matter including black carbon, Atmos. Chem. Phys., 17, 8681–8723, https://doi.org/10.5194/acp-17-8681-2017, 2017.

Kondo, Y., Sahu, L., Kuwata, M., Miyazaki, Y., Takegawa, N., Moteki, N., Imaru, J., Han, S., Nakayama, T., Oanh, N. T. K., Hu, M., Kim, Y. J., and Kita, K.: Stabilization of the Mass Absorption Cross Section of Black Carbon for Filter-Based Absorption Photometry by the use of a Heated Inlet, Aerosol Sci. Technol., 43, 741–756, https://doi.org/10.1080/02786820902889879, 2009.

Kondo, Y., Sahu, L., Moteki, N., Khan, F., Takegawa, N., Liu, X., Koike, M., and Miyakawa, T.: Consistency and traceability of black carbon measurements made by laser-induced incandescence, thermal-optical transmittance, and filter-based photo-absorption techniques, Aerosol Sci. Technol., 45, 295–312, https://doi.org/10.1080/02786826.2010.533215, 2011a.

Kondo, Y., Matsui, H., Moteki, N., Sahu, L., Takegawa, N., Kajino, M., Zhao, Y., Cubison, M. J., Jimenez, J. L., Vay, S., Diskin, G. S., Anderson, B., Wisthaler, A., Mikoviny, T., Fuelberg, H. E., Blake, D. R., Huey, G., Weinheimer, A. J., Knapp, D. J., and Brune, W. H.: Emissions of black carbon, organic, and inorganic aerosols from biomass burning in North America and Asia in 2008, J. Geophys. Res., 116, https://doi.org/10.1029/2010jd015152, 2011b.

Li, F., Zhang, X., Kondragunta, S., and Csiszar, I.: Comparison of fire radiative power estimates from VIIRS and MODIS observations, J. Geophys. Res., 123, 4545–4563, https://doi.org/10.1029/2017jd027823, 2018.

Lund, M. T., Samset, B. H., Skeie, R. B., Watson-Parris, D., Katich, J. M., Schwarz, J. P., and Weinzierl, B.: Short Black Carbon lifetime inferred from a global set of aircraft observations, npj Climate and Atmospheric Science, 1, 1–8, https://doi.org/10.1038/s41612-018-0040-x, 2018.

Matsui, H., Mori, T., Ohata, S., Moteki, N., Oshima, N., Goto-Azuma, K., Koike, M., and Kondo, Y.: Contrasting source contributions of Arctic black carbon to atmospheric concentrations, deposition flux, and atmospheric and snow radiative effects, Atmos. Chem. Phys., 22, 8989–9009, https://doi.org/10.5194/acp-22-8989-2022, 2022.

Miyazaki, Y., Kondo, Y., Sahu, L. K., Imaru, J., Fukushima, N., and Kano, M.: Performance of a newly designed continuous soot monitoring system (COSMOS), J. Environ. Monit., 10, 1195–1201, https://doi.org/10.1039/b806957c, 2008.

Mori, T., Kondo, Y., Ohata, S., Zhao, Y., Sinha, P. R., Oshima, N., Matsui, H., Moteki, N., and Koike, M.: Seasonal variation of wet deposition of black carbon in arctic Alaska, J. Geophys. Res., 125, https://doi.org/10.1029/2019jd032240, 2020.

Mouteva, G. O., Czimczik, C. I., Fahrni, S. M., Wiggins, E. B., Rogers, B. M., Veraverbeke, S., Xu, X., Santos, G. M., Henderson, J., Miller, C. E., and Randerson, J. T.: Black carbon aerosol dynamics and isotopic composition in Alaska linked with boreal fire emissions and depth of burn in organic soils, Global Biogeochem. Cycles, 29, 1977–2000, https://doi.org/10.1002/2015gb005247, 2015.

Ohata, S., Mori, T., Kondo, Y., Sharma, S., Hyvärinen, A., Andrews, E., Tunved, P., Asmi, E., Backman, J., Servomaa, H., and Others: Estimates of mass absorption cross sections of black carbon for filter-based absorption photometers in the Arctic, Atmos. Meas. Tech., 14, 6723–6748, https://doi.org/10.5194/amt-14-6723-2021, 2021.

Oshima, N., Yukimoto, S., Deushi, M., Koshiro, T., Kawai, H., Tanaka, T. Y., and Yoshida, K.: Global and Arctic effective radiative forcing of anthropogenic gases and aerosols in MRI-ESM2.0, Prog. Earth Planet. Sci., 7, 38, https://doi.org/10.1186/s40645-020-00348-w, 2020.

Overland, J. E., Wang, M., Walsh, J. E., and Stroeve, J. C.: Future Arctic climate changes: Adaptation and mitigation time scales, Earths Future, 2, 68–74, https://doi.org/10.1002/2013ef000162, 2014.

Pan, X., Kanaya, Y., Taketani, F., Miyakawa, T., Inomata, S., Komazaki, Y., Tanimoto, H., Wang, Z., Uno, I., and Wang, Z.: Emission characteristics of refractory black carbon aerosols from fresh biomass burning: a perspective from laboratory experiments, Atmos. Chem. Phys., 17, 13001–13016, https://doi.org/10.5194/acp-17-13001-2017, 2017.

Pan, X., Ichoku, C., Chin, M., Bian, H., Darmenov, A., Colarco, P., Ellison, L., Kucsera, T., da Silva, A., Wang, J., Oda, T., and Cui, G.: Six global biomass burning emission datasets: intercomparison and application in one global aerosol model, Atmos. Chem. Phys., 20, 969–994, https://doi.org/10.5194/acp-20-969-2020, 2020.

Paris, J.-D., Stohl, A., Nédélec, P., Arshinov, M. Y., Panchenko, M. V., Shmargunov, V. P., Law, K. S., Belan, B. D., and Ciais, P.: Wildfire smoke in the Siberian Arctic in summer: source characterization and plume evolution from airborne measurements, Atmos. Chem. Phys., 9, 9315–9327, https://doi.org/10.5194/acp-9-9315-2009, 2009.

Picotte, J. J., Bhattarai, K., Howard, D., Lecker, J., Epting, J., Quayle, B., Benson, N., and Nelson, K.: Changes to the Monitoring Trends in Burn Severity program mapping production procedures and data products, Fire Ecology, 16, 16, https://doi.org/10.1186/s42408-020-00076-y, 2020.

Polissar, A. V., Hopke, P. K., Malm, W. C., and Sisler, J. F.: The ratio of aerosol optical absorption coefficients to sulfur concentrations, as an indicator of smoke from forest fires when sampling in polar regions, Atmos. Environ., 30, 1147–1157, https://doi.org/10.1016/1352-2310(95)00334-7, 1996.

Polissar, A. V., Hopke, P. K., and Malm, W. C.: Atmospheric aerosol over Alaska: 1. Spatial and seasonal variability, J. Geophys. Res., https://doi.org/10.1029/98JD01365, 1998.

Quinn, P. K., Shaw, G., Andrews, E., Dutton, E. G., Ruoho-Airola, T., and Gong, S. L.: Arctic haze: current trends and knowledge gaps, Tellus B Chem. Phys. Meteorol., 59, 99, https://doi.org/10.1111/j.1600-0889.2006.00236.x, 2007.

Reap, R. M.: Climatological Characteristics and Objective Prediction of Thunderstorms over Alaska, Weather Forecast., 6, 309–319, https://doi.org/10.1175/1520-0434(1991)006<0309:CCAOPO>2.0.CO;2, 1991.

Rogers, H. M., Ditto, J. C., and Gentner, D.: Evidence for impacts on surface-level air quality in the northeastern US from long-distance transport of smoke from North American fires during the Long Island Sound Tropospheric Ozone Study (LISTOS) 2018, Atmos. Chem. Phys., 20, 671–682, https://doi.org/10.5194/acp-20-671-2020, 2020.

Sauvage, B., Fontaine, A., Eckhardt, S., Auby, A., Boulanger, D., Petetin, H., Paugam, R., Athier, G., Cousin, J.-M., Darras, S., and Others: Source attribution using FLEXPART and carbon monoxide emission inventories: SOFT-IO version 1.0, Atmos. Chem. Phys., 17, 15271–15292, https://doi.org/10.5194/acp-17-15271-2017, 2017.

Schmale, J., Arnold, S. R., Law, K. S., and Thorp, T.: Local Arctic air pollution: A neglected but serious problem, Earth's Future, https://doi.org/10.1029/2018EF000952, 2018.

Schmale, J., Zieger, P., and Ekman, A. M. L.: Aerosols in current and future Arctic climate, Nat. Clim. Chang., 11, 95–105, https://doi.org/10.1038/s41558-020-00969-5, 2021.

Selimovic, V., Yokelson, R. J., Warneke, C., Roberts, J. M., de Gouw, J., Reardon, J., and Griffith, D. W. T.: Aerosol optical properties and trace gas emissions by PAX and OP-FTIR for laboratory-simulated western US wildfires during FIREX, Atmos. Chem. Phys., 18, 2929–2948, https://doi.org/10.5194/acp-18-2929-2018, 2018.

Selimovic, V., Yokelson, R. J., McMeeking, G. R., and Coefield, S.: In situ measurements of trace gases, PM, and aerosol optical properties during the 2017 NW US wildfire smoke event, Atmos. Chem. Phys., 19, 3905–3926, https://doi.org/10.5194/acp-19-3905-2019, 2019.

Sharma, S., Ishizawa, M., Chan, D., Lavoué, D., Andrews, E., Eleftheriadis, K., and Maksyutov, S.: 16-year simulation of Arctic black carbon: Transport, source contribution, and sensitivity analysis on deposition, J. Geophys. Res., 118, 943–964, https://doi.org/10.1029/2012jd017774, 2013.

Sierra-Hernández, M. R., Beaudon, E., Porter, S. E., Mosley-Thompson, E., and Thompson, L. G.: Increased fire activity in Alaska since the 1980s: Evidence from an ice core-derived black carbon record, J. Geophys. Res., 127, https://doi.org/10.1029/2021jd035668, 2022.

Sinha, P. R., Kondo, Y., Koike, M., Ogren, J. A., Jefferson, A., Barrett, T. E., Sheesley, R. J., Ohata, S., Moteki, N., Coe, H., Liu, D., Irwin, M., Tunved, P., Quinn, P. K., and Zhao, Y.: Evaluation of ground-based black carbon measurements by filter-based photometers at two Arctic sites, J. Geophys. Res., 122, 3544–3572, https://doi.org/10.1002/2016jd025843, 2017.

Skamarock, W. C., Klemp, J. B., Dudhia, J., Gill, D. O., Liu, Z., Berner, J., Wang, W., Powers, J. G., Duda, M. G., Barker, D. M., and Others: A description of the advanced research WRF model version 4, National Center for Atmospheric Research: Boulder, CO, USA, 145, 2019.

Stein, A. F., Draxler, R. R., Rolph, G. D., Stunder, B. J. B., Cohen, M. D., and Ngan, F.: NOAA's HYSPLIT Atmospheric Transport and Dispersion Modeling System, Bull. Am. Meteorol. Soc., 96, 2059–2077, https://doi.org/10.1175/BAMS-D-14-00110.1, 2015.

Stohl, A., Andrews, E., Burkhart, J. F., Forster, C., Herber, A., Hoch, S. W., Kowal, D., Lunder, C., Mefford, T., Ogren, J. A., Sharma, S., Spichtinger, N., Stebel, K., Stone, R., Ström, J., Tørseth, K., Wehrli, C., and Yttri, K. E.: Pan-Arctic enhancements of light absorbing aerosol concentrations due to North American boreal forest fires during summer 2004, J. Geophys. Res., 111, https://doi.org/10.1029/2006jd007216, 2006.

Taketani, F., Miyakawa, T., Takashima, H., Komazaki, Y., Pan, X., Kanaya, Y., and Inoue, J.: Shipborne observations of atmospheric black carbon aerosol particles over the Arctic Ocean, Bering Sea, and North Pacific Ocean during September 2014, J. Geophys. Res., 121, 1914–1921, https://doi.org/10.1002/2015jd023648, 2016.

Taketani, F., Miyakawa, T., Takigawa, M., Yamaguchi, M., Komazaki, Y., Mordovskoi, P., Takashima, H., Zhu, C., Nishino, S., Tohjima, Y., and Others: Characteristics of atmospheric black carbon and other aerosol particles over the Arctic Ocean in early autumn 2016: Influence from biomass burning as assessed with observed microphysical properties and model simulations, Sci. Total Environ., 848, 157671, https://doi.org/10.1016/j.scitotenv.2022.157671, 2022.

Thackeray, C. W. and Hall, A.: An emergent constraint on future Arctic sea-ice albedo feedback, Nat. Clim. Chang., 9, 972–978, https://doi.org/10.1038/s41558-019-0619-1, 2019.

Vasileva, Moiseenko, and Skorokhod: Emission ratios of trace gases and particles for Siberian forest fires on the basis of mobile ground observations, Atmos. Chem. Phys., https://doi.org/10.5194/acp-17-12303-2017, 2017.

Wang, H., Rasch, P. J., Easter, R. C., Singh, B., Zhang, R., Ma, P.-L., Qian, Y., Ghan, S. J., and Beagley, N.: Using an explicit emission tagging method in global modeling of source-receptor relationships for black carbon in the Arctic: Variations, sources, and transport pathways, J. Geophys. Res., 119, 12,888-12,909, https://doi.org/10.1002/2014jd022297, 2014.

Wang, Q., Jacob, D. J., Fisher, J. A., Mao, J., Leibensperger, E. M., Carouge, C. C., Le Sager, P., Kondo, Y., Jimenez, J. L., Cubison, M. J., and Doherty, S. J.: Sources of carbonaceous aerosols and deposited black carbon in the Arctic in winter-spring: implications for radiative forcing, Atmos. Chem. Phys., 11, 12453–12473, https://doi.org/10.5194/acp-11-12453-2011, 2011.

653 van der Werf, G. R., Randerson, J. T., Giglio, L., van Leeuwen, T. T., Chen, Y., Rogers, B. M., Mu, M., van Marle, M. J. E.,
654 Morton, D. C., Collatz, G. J., Yokelson, R. J., and Kasibhatla, P. S.: Global fire emissions estimates during 1997–2016, Earth
655 Syst. Sci. Data, 9, 697–720, https://doi.org/10.5194/essd-9-697-2017, 2017.

656 van der Werf, G., Randerson, J. T., Giglio, L., Chen, Y., Rogers, B. M., and Van Leeuwen, T. T.: Global Fire Emissions
657 Database version 4 (GFED4), GC33D-0545, 2014.

658 Whaley, C. H., Mahmood, R., von Salzen, K., Winter, B., Eckhardt, S., Arnold, S., Beagley, S., Becagli, S., Chien, R.-Y.,
659 Christensen, J., and Others: Model evaluation of short-lived climate forcers for the Arctic Monitoring and Assessment
660 Programme: a multi-species, multi-model study, Atmos. Chem. Phys., 22, 5775–5828, https://doi.org/10.5194/acp-22-5775-
661 2022, 2022.

662 Wiggins, E. B., Soja, A. J., Gargulinski, E., Halliday, H. S., Pierce, R. B., Schmidt, C. C., Nowak, J. B., DiGangi, J. P., Diskin,
663 G. S., Katich, J. M., Perring, A. E., Schwarz, J. P., Anderson, B. E., Chen, G., Crosbie, E. C., Jordan, C., Robinson, C. E.,
664 Sanchez, K. J., Shingler, T. J., Shook, M., Thornhill, K. L., Winstead, E. L., Ziemba, L. D., and Moore, R. H.: High temporal
665 resolution satellite observations of fire radiative power reveal link between fire behavior and aerosol and gas emissions,
666 Geophys. Res. Lett., 47, https://doi.org/10.1029/2020gl090707, 2020.

667 Xie, A., Zhu, J., Kang, S., Qin, X., Xu, B., and Wang, Y.: Polar amplification comparison among Earth's three poles under
668 different socioeconomic scenarios from CMIP6 surface air temperature, Sci. Rep., 12, 16548, https://doi.org/10.1038/s41598-
669 022-21060-3, 2022.

670 Xu, J.-W., Martin, R. V., Morrow, A., Sharma, S., Huang, L., Leaitch, W. R., Burkart, J., Schulz, H., Zanatta, M., Willis, M.
671 D., Henze, D. K., Lee, C. J., Herber, A. B., and Abbatt, J. P. D.: Source attribution of Arctic black carbon constrained by
672 aircraft and surface measurements, Atmos. Chem. Phys., 17, 11971–11989, https://doi.org/10.5194/acp-17-11971-2017, 2017.

673 Yurganov, L. N., Jaffe, D. A., Pullman, E., and Novelli, P. C.: Total column and surface densities of atmospheric carbon
674 monoxide in Alaska, 1995, J. Geophys. Res., 103, 19337–19345, https://doi.org/10.1029/97jd02299, 1998.

675 Zheng, B., Ciais, P., Chevallier, F., Yang, H., Canadell, J. G., Chen, Y., van der Velde, I. R., Aben, I., Chuvieco, E., Davis, S.
676 J., Deeter, M., Hong, C., Kong, Y., Li, H., Li, H., Lin, X., He, K., and Zhang, Q.: Record-high CO2 emissions from boreal
677 fires in 2021, Science, 379, 912–917, https://doi.org/10.1126/science.ade0805, 2023.

678 Zhu, C., Kanaya, Y., Takigawa, M., Ikeda, K., Tanimoto, H., Taketani, F., Miyakawa, T., Kobayashi, H., and Pisso, I.:
679 FLEXPART v10.1 simulation of source contributions to Arctic black carbon, Atmos. Chem. Phys., 20, 1641–1656,
680 https://doi.org/10.5194/acp-20-1641-2020, 2020.

681